





# From Redshift to Real Space: Combining Linear Theory With Neural Networks

Edoardo Maragliano<sup>1,2</sup> , Punyakoti Ganeshaiah Veena<sup>1,2</sup> , Giulia Degni<sup>3</sup> , and Enzo Franco Branchini<sup>1,2</sup> 

<sup>1</sup> Department of Physics, Università di Genova, Via Dodecaneso 33, 16146 Genova, Italy

<sup>2</sup> Istituto Nazionale di Fisica Nucleare, Sezione di Genova, Via Dodecaneso 33, 16146 Genova, Italy

<sup>3</sup> Aix-Marseille Université, CNRS/IN2P3, CPPM, Marseille, France

July 16, 2025

## ABSTRACT

**Context.** Spectroscopic redshift surveys are designed to trace the large-scale structures (LSS) of the Universe and use its properties to test the validity of the  $\Lambda$ CDM model. However, using redshifts as distance proxies introduces distortions in the 3D mapping of galaxies which, if not accounted for, lead to systematic errors in the analysis of the LSS and the estimate of fundamental cosmological parameters.

**Aims.** To develop a new method combining linear theory (LT) and a neural network (NN) to mitigate redshift space distortions (RSDs), and to assess its effectiveness by applying it to a suite of dark matter halo catalogs.

**Methods.** We build and validate a hybrid reconstruction method (LT+NN) that combines linear density perturbation theory with an NN, trained using a Mean Squared Error (MSE) loss to map halo fields from redshift to real space. The training and validation is performed on halo fields extracted from  $z = 1$  snapshots of the Quijote N-body simulations. While the LT method is valid in the linear regime and corrects for large-scale distortions, the NN captures quasi-linear and smaller-scale features. Applying LT first and then training the NN on the corrected fields enables efficient and accurate reconstruction across scales.

**Results.** The MSE for the hybrid LT+NN method shows a substantial improvement of  $\sim 50\%$  over the LT and  $\sim 12\%$  over the NN reconstruction method. The LT+NN reconstructed fields show a tighter correlation to the real space fields compared to the other two. The improvement over the LT approach is also substantial in the halo-halo and halo-void correlation analyses, extending to scales as large as the BAO peak. Although the improvement over the NN method is less pronounced, it remains statistically significant, especially in reducing spurious anisotropies on large and quasi-linear scales, as quantified by the quadrupole moments of the correlation functions.

**Conclusions.** Our results illustrate that using a physically motivated approximate dynamical model before training an NN effectively overcomes the limitations of either approach when used in isolation. This hybrid method offers a superior way to mitigate RSDs, requiring only a relatively small training set and modest computational cost. This paves the way for future applications to more realistic datasets.

**Key words.** Cosmology - Large Scale Structures Reconstruction - Machine Learning

## 1. Introduction

The need to address fundamental problems in physics, such as the origin of the accelerated expansion of the Universe, the nature of dark matter, and the mass of neutrinos, has led to the design and execution of galaxy redshift surveys covering increasingly large volumes. The motivation behind this is that the spatial distribution and evolution of cosmic structures, collectively known as the large-scale structure of the Universe, encode the information necessary to tackle and potentially resolve these open questions. Effective extraction of that information from these large datasets has become one of the key issues in observational cosmology.

One prominent example is the Baryon Acoustic Oscillation (BAO) feature observed in the galaxy-galaxy correlation function. First detected in the SDSS Luminous Red Galaxy sample (Eisenstein et al. 2005), the BAO has since become one of the most powerful cosmological probes for tracing the expansion history of the Universe. This is evidenced by the consistent and robust results obtained from a wide range of BAO analyses over the years, culminating in the most recent measurements from DESI (DESI Collaboration et al. 2025).

Along with the improvements in both the quality and the quantity of data expected from ongoing and planned surveys (Mellier et al. 2025; Ivezić et al. 2019; Dore et al. 2019), the demand for greater precision and accuracy has increased in parallel. Taking the BAO example, achieving a more precise measurement of the peak location, amplitude, and anisotropy requires not only a reduction in statistical errors, achievable by increasing the survey volume and the number of galaxies, but also improved control over systematic uncertainties. These systematics can arise from instrumental effects, observational strategies, and astrophysical processes. Furthermore, they may depend on the very cosmological model one aims to constrain. This is particularly true when using observed redshifts as distance proxies, or when modeling the complex physics that governs the evolution of LSS, especially in the nonlinear regime where galaxy formation and its relation to the underlying matter density field become increasingly difficult to predict.

Broadly speaking, two strategies can be adopted to correct for cosmology-dependent systematic uncertainties: forward and inverse modeling. Reconstruction methods fall into the latter category. These aim to infer the past trajectories of galaxies from their present-day distribution in redshift space, under the as-

sumption that the initial matter distribution was homogeneous. This process necessarily involves theoretical assumptions, such as the use of the Zel’dovich approximation (ZA) (Zel’dovich 1970; Nusser & Davis 1994), the minimization of a cost function in the context of the mass transportation problem (Frisch et al. 2002), or the extremization of a suitably defined cosmological action with respect to a set of trial orbits (Peebles 1989) to quote the most relevant.

Thanks to more efficient implementations and reduced computational costs, these reconstruction methods have been successfully applied to increasingly large datasets. Returning to the BAO example, they have significantly enhanced the signal-to-noise ratio of the BAO peak, leading to improved estimates of cosmological parameters (see, e.g., Padmanabhan et al. (2012); Sarpa et al. (2019); Nikakhtar et al. (2023), and references therein). As a result, reconstruction methods are now routinely employed in galaxy clustering analyses – primarily in their Lagrangian, “Zel’dovich” implementations (Padmanabhan et al. 2012; White 2015; Burden et al. 2015) – as demonstrated, for example, in the recent analysis of DESI data (Paillas et al. 2025).

Machine learning (ML) methods provide an alternative to traditional reconstruction techniques, as they do not require explicit assumptions about the physical relationship between the observed and reconstructed fields. Moreover, they offer a natural framework to correct for observational systematics, provided these effects are properly incorporated into the training data. These advantages, combined with the growing availability of high-quality N-body simulations for training (Villaescusa-Navarro et al. 2020, 2021), are the main reasons behind the increasing interest in ML and its application to cosmological reconstruction.

The ability of neural network (NN)-based methods to reconstruct the underlying matter and velocity fields from the distribution of matter, dark matter halos or mock galaxies has been demonstrated using simulated datasets (Hong et al. 2021; Wu et al. 2023; Ganeshiah Veena et al. 2023; Lilow et al. 2024; Wang & Yang 2024; Du et al. 2025; Shi et al. 2025). These methods have also proven successful in tracing the positions of cosmic objects back in time (Shallue & Eisenstein 2023; Chen et al. 2023; Chen et al. 2024; Parker et al. 2025). Furthermore, they have been applied to real observational data, such as 2MRS (Lilow et al. 2024) and SDSS DR7 (Wang & Yang 2024), effectively accounting for the survey selection function and recovering the nonlinear relationship between the density and peculiar velocity fields.

Here, we focus on a specific aspect of reconstruction methods: their ability to predict the impact of peculiar velocities and, therefore, to remove the so-called redshift-space distortions (Hamilton 1998) from the three-dimensional mapping of galaxy positions in spectroscopic redshift surveys. Accurately modeling RSDs is crucial for robust cosmological inference. In clustering analyses they are often modeled by combining linear perturbation theory (Kaiser 1987) to describe the effect of coherent flows on large scales with a phenomenological treatment of incoherent motions within virialised structures, also known as *Finger-of-God* effect (Jackson 1972). ML-based reconstruction methods offer a significant improvement in this context due to their ability to model peculiar velocities in the mildly nonlinear regime (Ganeshiah Veena et al. 2023; Wu et al. 2023; Wang & Yang 2024; Shi et al. 2025).

In this work, we adopt a two-step hybrid procedure, similar to the one proposed by Parker et al. (2025), which combines the Lagrangian iterative method based on the Zel’dovich approximation (Burden et al. 2015), commonly used to remove nonlinear

effects around BAO scales, with the neural network reconstruction technique employed by (Ganeshiah Veena et al. 2023) to account for nonlinear distortions on smaller scales. The goal is to remove RSDs from the observed three-dimensional distribution of a set of mass tracers, which in our case are dark matter halos extracted from a suite of QUIJOTE N-body simulations (Villaescusa-Navarro et al. 2020).

To assess the quality of the reconstruction, we compare the performance of the hybrid approach against that of the standard iterative method which we dub LT since it ultimately assumes linear perturbation theory, and the NN-based reconstruction alone. We shall refer to the hybrid approach as the LT+NN method. In particular, we evaluate their respective abilities to recover the halo-halo two-point statistics – both in configuration and Fourier space – and to remove RSDs from the average shape of cosmic voids.

Since our goal is to assess the relative effectiveness of the three methods in removing RSDs, we employ the same cosmological model used in the QUIJOTE simulations for all reconstructions. As a result, our analysis does not account for potential systematic errors that could arise from adopting an incorrect cosmological model to convert redshifts into distances (Alcock & Paczynski 1979), or, in the case of LT reconstruction, from using incorrect values for the linear growth rate and/or halo bias.

The layout of the article is as follows. In Sec. 2, we describe the mock datasets used in our analysis and their parent N-body simulations. In Sec. 3, we present the three reconstruction methods employed in this work: the Lagrangian iterative method, the neural network-based method, and the hybrid LT+NN approach.

The results of our analysis are provided in Sec. 4. We begin by assessing the quality of the reconstructions through visual inspection, point-by-point comparisons, and one-point statistics. We then analyze two-point summary statistics, including the halo-halo two-point correlation function, the power spectrum, and the cross-correlation between the Fourier coefficients of the reconstructed and true density fields.

Finally, we extract cosmic voids from both the true and reconstructed fields, measure their void-galaxy cross correlation function and evaluate each method’s ability to recover the undistorted void density profile. Our discussion and conclusions are presented in Sec. 5.

## 2. Simulation mocks for training

The QUIJOTE simulations (Villaescusa-Navarro et al. 2020) are a large suite of cosmological N-body simulations designed for machine learning applications in cosmology. They provide both a massive and diverse dataset, as well as high-precision outputs, making them particularly suitable for training neural networks in large-scale structure analyses

In this work, we use a subsample of the fiducial QUIJOTE suite at redshift  $z = 1$ , consisting of 100 high-resolution simulations. Each simulation box contains  $1024^3$  particles within a comoving volume of  $1000 h^{-1}$  Mpc on a side, with a particle mass of  $8.2 \times 10^{10} M_{\odot} h^{-1}$ . The initial conditions at  $z = 127$  were generated using second-order Lagrangian Perturbation Theory (2LPT). The cosmological parameters assumed in the simulations are listed in Tab. 1.

In this work we use the public dark matter halo catalogues extracted from the QUIJOTE simulations using the Friends-of-Friends (FoF) algorithm. Each halo is composed of at least 20 particles, which corresponds to a minimum halo mass of  $1.64 \times 10^{12} M_{\odot} h^{-1}$ . The most massive halos reach up to  $9.555 \times 10^{14} M_{\odot} h^{-1}$ , corresponding to approximately  $10^4$  particles. The

$\Omega_m$	$\Omega_b$	$h$	$n_s$	$\sigma_8$
0.3175	0.049	0.6711	0.9624	0.834

**Table 1.** Cosmological parameters of the fiducial QUIJOTE simulations.

resulting number density of halos is approximately  $2.39 \times 10^{-3} h^3 \text{Mpc}^{-3}$ , significantly higher than that of existing and ongoing wide spectroscopic galaxy redshift survey.

### 2.1. Input and target fields

For each of the 100 available mock catalogs at  $z = 1$ , we generate the corresponding redshift-space catalogs by adopting the distant observer approximation and shifting halos from their real-space coordinate  $\mathbf{x}$  to the redshift-space one  $\mathbf{s}$  according to

$$\mathbf{s} = \mathbf{x} + \frac{v_z}{H} \hat{\mathbf{z}} \quad (1)$$

where  $v_z$  is the peculiar velocity of the halo along the  $z$ -axis direction  $\hat{\mathbf{z}}$  and  $H$  is the Hubble constant. Periodic boundary conditions are applied to preserve the shape of the cubic box.

We estimate the halo number density field on a  $128^3$  cubic grid using Cloud-in-Cell interpolation from halo positions, resulting in 100 independent realizations of the density field in both real and redshift space. The chosen grid size,  $\Delta x \approx 7.8 h^{-1} \text{Mpc}$ , ensures an average of one halo per cell. This choice represents a reasonable compromise between minimizing shot noise, avoiding the oversmoothing of small-scale features, and reducing the computational cost of the neural network reconstruction.

## 3. Reconstruction techniques

In this section, we present the three reconstruction methods used in this work to correct for RSDs.

### 3.1. Linear Theory reconstruction [LT]

The first method relies on linear perturbation theory to correct for RSDs. The displacement field,  $\Psi = \mathbf{x} - \mathbf{q}$ , is estimated from the redshift-space overdensity field, defined as  $\delta_{\text{obs}} = \frac{\rho(\mathbf{s}) - \bar{\rho}}{\bar{\rho}}$ , where  $\rho$  is the number density of halos,  $\mathbf{s}$  is the position in redshift space, and  $\mathbf{q}$  is the position in real space. To estimate  $\Psi$ , the linearized continuity equation (Nusser & Davis 1994) is solved,

$$\nabla \cdot \Psi + \beta \nabla \cdot (\Psi \cdot \hat{\mathbf{r}}) \hat{\mathbf{r}} = -\frac{\delta_s}{b}. \quad (2)$$

Here  $\hat{\mathbf{r}}$  is the line-of-sight unit vector, and  $\beta = f/b$  is the ratio of the linear growth rate  $f$  to the linear bias  $b$ .

We solve this equation in Fourier space using the iterative procedure introduced by Burden et al. (2015), which repeatedly applies the Fast Fourier Transform technique. In this process, we do not use the halo number density estimated on the  $128^3$  grid,  $\delta_{\text{obs}}$ , as the source term; instead, we use its smoothed version:

$$\delta_s(k) = \exp \left[ -\frac{1}{2} \left( \frac{k}{R_s} \right)^2 \right] \delta_{\text{obs}}(k), \quad (3)$$

where  $\delta(k)$  denotes the Fourier coefficients of the overdensity field, and  $R_s$  is the radius of the adopted Gaussian smoothing filter. The smoothing radius is a free parameter of the reconstruction. Its value is not known *a priori*, but depends on the

characteristics of the catalog and, in principle, on the properties of the reconstructed field one is most interested in. We use  $R_s = 10 h^{-1} \text{Mpc}$  – a value slightly larger than the cell size – as a reference, since, as we will show in Sec. 4, it proves more effective at removing RSDs from two-point clustering statistics. We will test the sensitivity of the reconstruction to the smoothing radius in Sec. 4.3.

The resulting displacement field  $\Psi$ , specified at the  $128^3$  grid points, is CIC-interpolated at the redshift-space positions of the halos. Using linear theory, these halos are then displaced by  $-f(\Psi \cdot \hat{\mathbf{z}}) \hat{\mathbf{z}}$  to their reconstructed positions in the real space, imposing periodic boundary conditions.

Finally, the reconstructed real-space halo density field is obtained by interpolating the halo positions onto the  $128^3$  grid.

To perform the reconstruction, both the linear growth rate  $f$  and the linear bias  $b$  of the halos must be specified. We estimate an effective  $b$  value from the ratio of the halo and matter power spectra computed in the 100 mock catalogs.

$$b = \left\langle \sqrt{\frac{P_{\text{halo}}(k)}{P_{\text{matter}}(k)}} \right\rangle, \quad (4)$$

where the average is taken over modes with  $k < k_{\text{max}} = 0.07 h \text{Mpc}^{-1}$ , where this ratio remains approximately constant and the linear bias approximation holds. The linear growth rate value is set equal to the simulation value  $f \simeq \Omega_m(z = 1)^{0.55} = 0.88$ .

### 3.2. Neural network reconstruction [NN]

A neural network is generally defined as a computational model designed to predict targets from input data, using adjustable weights and biases that are fine-tuned by minimizing a loss function. To achieve this, we apply the autoencoder-based technique described in Ganeshiah Veena et al. (2023) and Lilow et al. (2024), using a similar architecture with a few modifications. A detailed description of the neural network procedure can be found in Ganeshiah Veena et al. (2023); here, we summarize only the main concepts.

The NN model is constructed using a symmetric encoder-decoder scheme that captures hierarchical features through successive downsamplings and reconstructs the fields using corresponding upsampling paths with skip connections.

The encoder consists of five convolutional blocks, each comprising two 3D convolutional layers with Rectified Linear Unit [ReLU] activation and same padding, followed by a 3D max pooling layer with a stride of (2, 2, 2). The use of convolutional layers with padding ensures that features of the density fields are learned without reducing spatial dimensions, while the max pooling layers serve to downsample the input volume and reduce its size. The number of filters increases progressively from 16 to 256 along the encoding path, enabling the network to capture increasingly abstract representations at deeper layers. The choice of filter counts and other hyperparameters was guided by a trade-off between model complexity (i.e., the number of trainable parameters) and the corresponding improvement in the loss function.

The decoder mirrors the encoder in structure and is composed of a series of upsampling blocks. Each block begins with two 3D convolutional layers that refine the feature representations. This is followed by a 3D transposed convolution layer (also known as deconvolution), which up-samples the feature maps to a higher spatial resolution. To preserve spatial context and improve reconstruction accuracy, the upsampled fea-



ture maps are concatenated with the corresponding feature maps from the encoder through skip connections. These skip connections help recover fine-grained details lost during downsampling in the encoder.

The final layer of the network is a 3D convolutional layer followed by a ReLU activation function. This layer produces the output 3D field, maintaining the same spatial dimensions as the input volume. The ReLU activation ensures that the predicted density values remain physically plausible by preventing negative densities. The entire architecture is fully convolutional, designed to operate on input volumes consisting of  $128^3$  grids. The model contains approximately  $8.3 \times 10^6$  trainable parameters.

### 3.2.1. Training and loss

To train the neural network reconstruction, we use 80 out of 100 available redshift-space halo number density fields, denoted  $\rho_j^{\text{obs},\alpha}$ , along with their corresponding real-space halo number density fields,  $\rho_j^{\text{real},\alpha}$ . Here  $\alpha = 1, \dots, M_{\text{train}}$  indexes the field realizations used for training, and  $j = 1, \dots, M_{\text{grid}} = 128^3$  indexes the grid cells within each volume.

During training, the hyperparameters of the network are adjusted to minimize a chosen loss function. This optimization is performed using a method known as stochastic gradient descent (SGD) (Goodfellow et al. 2016). In SGD, the training dataset is divided into small subsets called mini-batches, which are processed sequentially. For each mini-batch, the average gradient of the loss function is computed and used to update the model parameters via backpropagation. These updated parameters are then used for the next mini-batch. This procedure iterates over all training samples in what is known as an epoch. Training continues for multiple epochs until the loss stabilizes and converges.

For this paper, we used the mean squared error (MSE) loss function

$$\text{MSE}(\hat{\rho}^{\text{NN}}) = \frac{1}{M_{\text{train}} M_{\text{grid}}} \sum_{\alpha=1}^{M_{\text{train}}} \sum_{j=1}^{M_{\text{grid}}} (\rho_j^{\text{real},\alpha} - \hat{\rho}_j^{\text{NN},\alpha})^2, \quad (5)$$

with  $\hat{\rho}$  representing the reconstructed field. A network that minimises the MSE loss, estimates the mean of the posterior distribution, which is the mean of all true fields, given the observed fields (Goodfellow et al. 2016; Ganeshiah Veena et al. 2023).

As anticipated, we use 80 realisations out of the total 100 for training, with the remaining 20 used for validation and testing. The training is run for up to 1000 epochs. Our network was trained on NVIDIA L40S GPUs with 48GB RAM. For 1000 epochs, the training took around 2 to 5 hours, wall clock time, depending on the availability of the GPUs.

In Fig. 1, we compare the value of the loss function,  $\text{MSE}(\hat{\rho})$ , as a function of training epochs for both the training set (blue dots connected by a continuous curve) and the validation set (blue crosses connected by a continuous curve).

While the MSE for the validation set begins to flatten after approximately 500 epochs, the training set curve continues to decrease steadily. This divergence is a characteristic signature of overfitting, likely caused by the limited size of the training dataset.

For reference, we also show the  $\text{MSE}(\hat{\rho})$  computed from the LT-reconstructed halo density field (horizontal grey line). This value is higher than that achieved by the NN-based reconstruction, indicating that the neural network yields a more accurate reconstruction than LT alone. A detailed comparison between the two reconstruction methods will be presented in the next section.

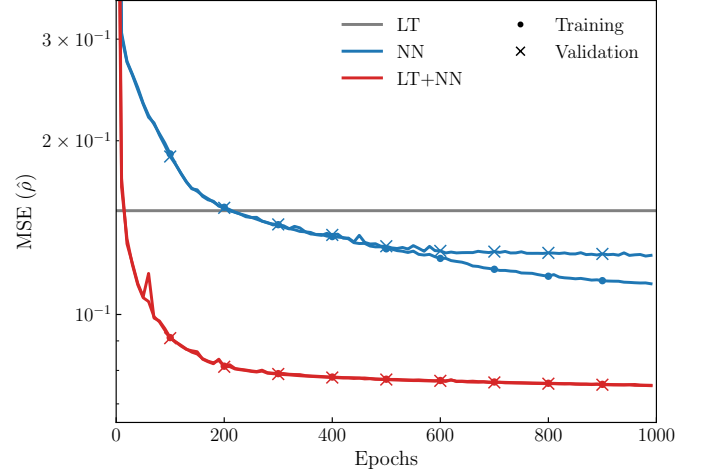


**Fig. 1.** MSE values as a function of training epochs are shown for the different reconstruction methods considered in this work: NN (blue symbols and curves), LT+NN (red), and LT (grey horizontal line). Dots and crosses indicate results obtained with the training and validation sets, respectively. LT reconstructions were performed using Gaussian smoothing with a radius of  $R_s = 10 h^{-1}$  Mpc.

### 3.3. Hybrid reconstruction [LT+NN]

The third reconstruction method we present is a hybrid approach that combines linear reconstruction with neural network reconstruction. Specifically, the method first applies a LT reconstruction step, and then uses the resulting density field as input to the NN. In practice, this means the NN is fed a different observed density field,  $\rho_j^{\text{obs}}$ , still defined on a  $128^3$  cubic grid.

This hybrid approach introduces only a minimal computational overhead, as the LT reconstruction is a fast, deterministic operation that requires significantly less time and memory than training or running the neural network. In typical cases, the LT step completes in a few seconds to minutes, depending on implementation and hardware, making it a practical addition to the pipeline.

The corresponding MSE curves for the hybrid reconstruction are shown in Fig. 1 (red symbols). In this case, the training and validation curves (dots and crosses) nearly coincide and both flatten after approximately 400 epochs. They reach a value significantly lower than that of the NN-only reconstruction, indicating a further improvement in reconstruction quality. We interpret the lack of overfitting as a result of the LT step successfully modeling coherent RSDs on large scales, leaving the neural network to focus solely on removing small-scale RSD.

## 4. Results

The MSE values of the reconstructed fields shown in Fig. 1 serve as a proxy for the quality of the reconstruction. Our results show that the NN method performs better than the one based on the linear theory approximation, as expected. However, the improvement in terms of the asymptotic MSE value is relatively modest ( $\sim 13\%$ ). A significantly larger improvement is achieved with the hybrid LT+NN approach, which leads to a 50% reduction in the asymptotic MSE compared to the LT method.

Although MSE is a useful proxy, it represents an average over the entire density field and therefore cannot fully capture the quality of the reconstructions. To complement this, a qualitative inspection of the appearance of the reconstructed density field

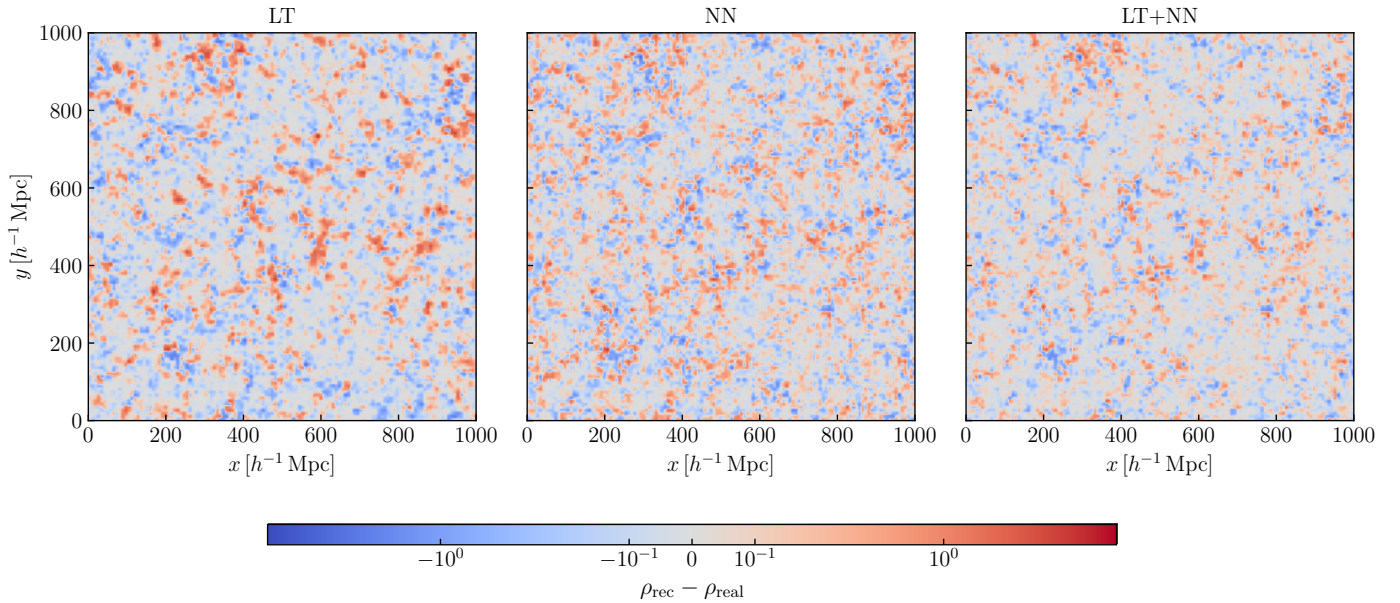


**Fig. 2.** Residuals between the density field obtained with the three reconstruction methods, identified by the top labels, and the real space one. The plots show the density in a slice of  $7.8 h^{-1}$  Mpc from one of the validation set, extracted across the  $z$  axis of the cube, expressed in number of halos per cell.

can provide valuable insights. For this reason, we show in Fig. 2 the residuals between one of the reconstructed fields and its corresponding true density fields for the LT (left panel), NN (middle panel), and LT+NN (right panel) methods. Different shades of red and blue indicate the magnitude of positive and negative residuals, respectively, as shown in the color scale in the bottom bar. The residuals steadily decrease from left (LT reconstruction) to right, confirming that the hybrid LT+NN reconstruction provides the best results.

To provide a more quantitative assessment, we compare the reconstructed  $\rho$  values at the grid point positions with the true ones for each of the three reconstruction methods in Fig. 3 by sampling from all 20 available validation fields.

We choose to plot the true density, versus the reconstructed one, since the regression of  $\rho_{\text{real}}$  on  $\hat{\rho}_{\text{NN}}$  is expected to yield a slope of unity – as shown by Ganeshiah Veena et al. (2023). This is a consequence of the NN trained on an MSE loss, which estimates the mean of the conditional distribution, i.e.,  $\hat{\rho}_{\text{NN}} = \langle \rho_{\text{real}} | \rho_{\text{obs}} \rangle$ . The Pearson correlation coefficients, estimated from the scatter plots, are reported in the figure labels. The results show that the LT method systematically overestimates the amplitude of the reconstructed density in both high- and low-density regions (grey dots). This bias and the scatter are significantly reduced in the NN (blue) and LT+NN (red) cases. Moreover, the LT+NN approach yields a Pearson coefficient closer to unity, indicating a more accurate reconstruction.

The values of the mean halo number density, variance, and the Pearson correlation coefficients obtained from stacking the 20 reconstructions are reported in Tab. 2. We show two sets of Pearson coefficients: those estimated from the true versus reconstructed regression and those from the reconstructed versus true regression. In addition, the scatter around the diagonal, defined as the root mean square of the residuals between reconstructed and true densities, is reported for each case.

To further investigate and characterise the relative and absolute performance of the three reconstruction methods in removing redshift-space distortions, we now turn our attention to three

	Real space	LT	NN	LT+NN
$\langle \rho \rangle$	1.14	1.14	1.14	1.14
$\sigma^2(\rho)$	1.60	1.91	1.47	1.52
$r_{\text{real v/s recon}}$	–	0.96	0.96	0.98
$r_{\text{recon v/s real}}$	–	0.96	0.96	0.98

**Table 2.** Mean, variance and Pearson correlation coefficient of the real and reconstructed halo number density fields from the three methods (LT, NN, LT+NN), computed over 20 mock realizations. The LT reconstruction uses a smoothing scale of  $R_s = 10 h^{-1}$  Mpc. The fields represent the number of halos per grid cell; physical densities in  $(h^{-1} \text{ Mpc})^{-3}$  can be obtained by dividing by the cell volume, with a length of  $7.8 h^{-1}$  Mpc.

summary statistics that are widely used as cosmological probes in galaxy clustering analyses.

The first is the one-point probability distribution function (PDF) of the reconstructed galaxy density field, which offers a more detailed view of the point-by-point comparison shown in the scatter plots. The first and second moments of this distribution are listed in Tab. 2.

The second is the two-point clustering statistic, which we compute both in configuration space (i.e., the halo-halo two-point correlation function) and in Fourier space (i.e., the halo power spectrum).

Finally, we also consider cosmic voids extracted from the reconstructed halo catalogs. We assess the quality of the reconstructions by examining the average void shape, as traced by the void-halo cross-correlation function.

#### 4.1. The 1-point halo density probability distribution function

The one-point PDFs of the three reconstructed halo density fields are shown in Fig. 4, alongside the true distribution for comparison, using both log-log (upper panel) and lin-log (lower panel) scales to better highlight the differences. The color scheme fol-

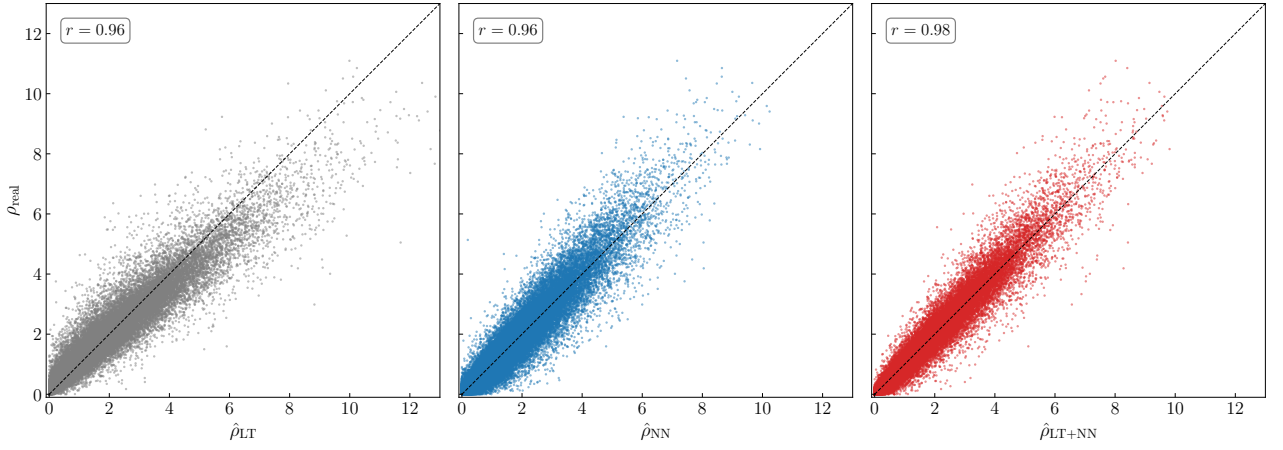


**Fig. 3.** Scatter plot of the true vs. the reconstructed halo number density – in units of halos per cell – measured at the points of the  $128^3$  grid for the three reconstruction methods considered: LT (left), NN (middle) and LT+NN (right). The plot has been made by sampling points from the 20 fields of the validation set.

lowers that used in the previous plots. The results confirm the qualitative analysis from the scatter plot, indicating that the LT method (grey curves) systematically overestimates the absolute amplitude of the reconstructed density in both high- and low-density regions. As a consequence, it also distorts the evaluation of the halo density when it is close to the cosmic mean.

In contrast, the NN reconstruction (blue) systematically assigns a density close to the mean in regions that are actually underdense, as the NN reconstruction is the mean posterior estimate of true fields given the observed field, and this approaches the mean field when there is no signal (tracers).

The PDF of the LT+NN reconstructed field (red), on the other hand, provides an excellent match to the true distribution across the entire density range, confirming the initial positive impression from the visual inspection of the density maps and scatter plots.

#### 4.2. Two-point statistics

Two-point statistics are the primary tool in galaxy clustering analyses. Since the goal of our reconstruction is to remove redshift-space distortions, we focus on the monopole and quadrupole moments of the anisotropic two-point statistics, evaluated in both Fourier and configuration space.

We begin with the power spectrum of the halo density field, defined as the expectation value of the squared modulus of the Fourier coefficients  $\delta_h(\mathbf{k})$ , estimated from  $128^3$  grid points using the `MeshFFTPower` class from the public code `PyPower` (Hand et al. 2017):

$$\langle \delta_h(\mathbf{k}) \delta_h^*(\mathbf{k}') \rangle = (2\pi)^3 \delta_D(\mathbf{k} - \mathbf{k}') P_h(\mathbf{k}). \quad (6)$$

Multipoles are estimated as follows,

$$P_\ell(k) = \frac{2\ell + 1}{2} \int_{-1}^1 P(k, \mu) \mathcal{L}_\ell(\mu) d\mu, \quad (7)$$

where  $\mathcal{L}_\ell(\mu)$  are Legendre polynomials and  $\mu = \hat{\mathbf{k}} \cdot \hat{\mathbf{z}}$ . We only consider the  $\ell = 0$  and the  $\ell = 2$  cases.

The results, averaged over the 20 reconstructions, are shown in Fig. 5, using the same color scheme as in the previous plots.

The monopole moment of the LT-reconstructed field (grey curve in the top-left panel) is systematically higher than in all other cases, including the reference case (black curve). To better illustrate the mismatch, we show in the bottom panel the

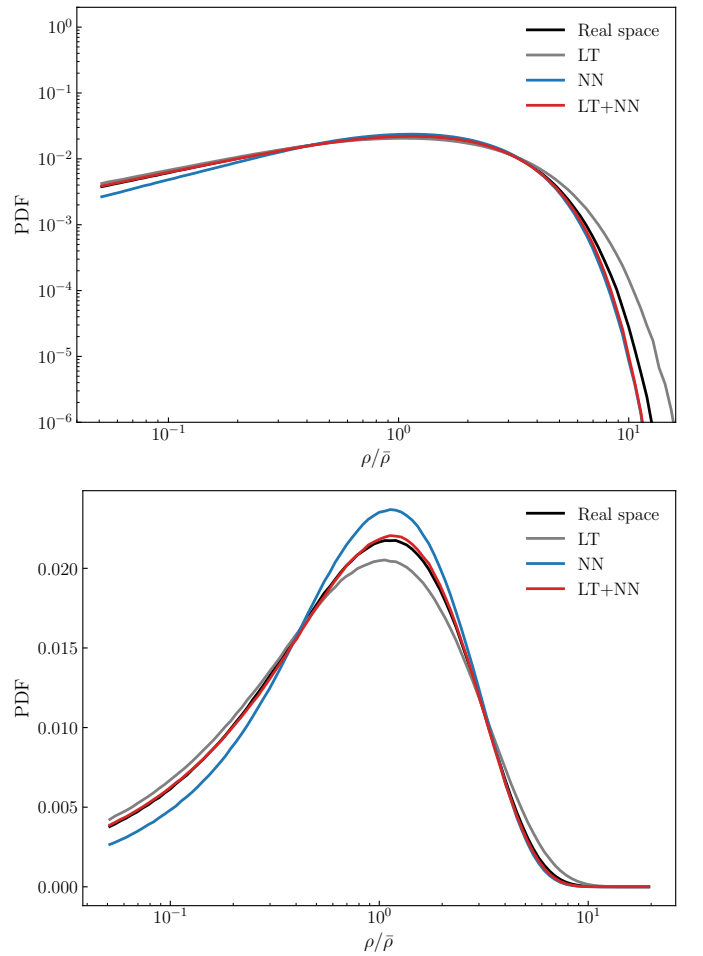


**Fig. 4.** The PDFs of the reconstructed density fields, normalized by the mean, for the three methods (LT, NN, and LT+NN) are shown alongside the true distribution and labeled accordingly. The plot shows the average over 20 validation samples. The upper and lower panels display the same curves in log-log and lin-log scales, respectively, to better highlight discrepancies.

monopole residuals with respect to the reference (true) case, averaged over the 20 reconstruction sets. These are over-plotted with two horizontal grey bands representing the level of the



RMS scatter and twice that amount among the 20 measurements, which we refer to as the  $1\sigma$  and  $2\sigma$  scatter, respectively.

The results indicate that the LT reconstruction systematically overestimates the clustering amplitude across all scales, with the bias becoming more pronounced toward smaller scales. This probably stems from the fact that linear theory underestimates the displacement length along straight-line orbits and, consequently, the halo peculiar velocities. As a result, redshift-space distortions are not fully removed, leading to spurious enhancement of the clustering amplitude. This effect is less significant on large scales, where linear theory provides a better approximation, and becomes more pronounced on smaller scales, where nonlinear effects dominate.

According to this interpretation, the imperfect removal of RSDs would also violate statistical isotropy, potentially leaving behind a spurious quadrupole signal. In fact, this is observed in the right panel: the quadrupole moment of the power spectrum is systematically greater than zero, with an approximately constant amplitude over the range  $k = [0.04, 0.2] h \text{ Mpc}^{-1}$ .

In comparison, the NN reconstruction is significantly more effective than LT in recovering the monopole signal on most scales, except for the largest ones. We attribute this limitation, clearly visible as a residual, negative quadrupole moment, to the restricted size of the training set, since each of the 80 available catalogs contains a limited number of large-scale Fourier modes for the network to learn from. The net result is that the NN reconstruction outperforms LT in reducing the overall clustering amplitude, but performs less satisfactorily at  $k < 0.03 h \text{ Mpc}^{-1}$ .

However, in terms of absolute performance, the amplitude of the residual RSD signal is non-negligible, exceeding  $2\sigma$  across a significant range of wavenumbers in both the monopole and quadrupole residuals. Finally, the residuals become significantly negative in both moments on small scales ( $k \geq 0.2 h \text{ Mpc}^{-1}$ ), a feature we interpret as the combined effect of grid resolution and Gaussian smoothing. These factors do not fully remove small-scale RSDs and contribute to the characteristic elongation of structures along the line of sight, commonly referred to as the Fingers-of-God effect.

By far the best results are achieved with the LT + NN reconstruction, which, as clearly shown in the plot, provides an excellent match to the true power spectrum monopole and quadrupole throughout the  $k$  range up to  $k = 0.2 h \text{ Mpc}^{-1}$ . In particular, the consistency of the quadrupole with zero highlights the effectiveness of the hybrid approach in removing redshift-space distortions.

To offer a complementary view of the reconstruction performance and to highlight the importance of recovering the BAO peak, we repeated the same analysis in configuration space, using two-point correlation statistics instead of the power spectrum. The two-point correlation function of the halo overdensity field  $\delta_h(\mathbf{x})$ , estimated on the  $128^3$  grid, is defined as the expectation value of the pair products:

$$\xi_h(\mathbf{r}) = \langle \delta_h(\mathbf{x}) \delta_h(\mathbf{x} + \mathbf{r}) \rangle, \quad (8)$$

where  $\mathbf{r}$  is the pair separation vector.

We estimate the anisotropic 2PCF in radial bins of width  $2.5 h^{-1} \text{ Mpc}$  over the range  $|\mathbf{r}| \in [0, 200] h^{-1} \text{ Mpc}$ , and in 200  $\mu$  bins, where  $\mu = \cos \theta$  and  $\theta$  is the angle between pair separation vectors and the line of sight to the pair. We always identify the line of sight with the  $z$ -axis, adopting the distant observer approximation. The  $\mu$  bin is set to  $\Delta\mu = 0.01$  over the interval  $[-1, 1]$ . We notice that the width of the radial bin is smaller than the cell size.

As for the power spectrum case, we will focus on the monopole and quadrupole moments of the 2PCF defined in analogy with Eq. (7).

The results are summarized in Fig. 6, which follows the same format as Fig. 5 and conveys similar information. As expected, the LT method yields the poorest 2PCF reconstruction. In the monopole, the amplitude of its residuals exceeds  $2\sigma$  at separations smaller than  $r \approx 75 h^{-1} \text{ Mpc}$  and, which is most worrying, in correspondence of the BAO peak. Only on scales larger than  $r \approx 150 h^{-1} \text{ Mpc}$  residuals converge to zero, in both the monopole and quadrupole moments.

The NN reconstruction performs significantly better. The monopole residuals remain within the  $1\sigma$  band across nearly all scales, except at the smallest separations ( $r < 20 h^{-1} \text{ Mpc}$ ). However, the quadrupole moment of the NN-reconstructed 2PCF deviates significantly from zero on almost all scales, consistent with the findings from the Fourier-space analysis (note that the quadrupole moments of the power spectrum and the two-point function have opposite signs by definition).

Finally, as expected, the LT+NN reconstruction accurately removes the RSD effects across all scales, including at the BAO peak, and remains reliable down to  $r \approx 20 h^{-1} \text{ Mpc}$ .

To further assess the quality of our reconstruction, we compute the cross-correlation coefficient in Fourier space, defined as

$$r(k) = \frac{P_{\text{true,rec}}(k)}{\sqrt{P_{\text{rec}}(k)P_{\text{true}}(k)}}, \quad (9)$$

where  $P_{\text{rec,true}}(k)$  is the cross power spectrum between the true and reconstructed halo density fields and where  $P_{\text{rec}}$  and  $P_{\text{true}}$  are their respective auto power spectra.

This coefficient quantifies how well the phases of the reconstructed halo field match those of the true (RSD-free) halo field. The results are shown in Fig. 7 as three continuous curves, plotted using the standard color scheme.

All curves exhibit a similar trend: they remain close to unity on large scales – where the removal of redshift-space distortions is expected to be more accurate – and gradually deviate from this value at smaller scales, followed by a sharp drop where nonlinear effects become increasingly difficult to model and subtract.

However, the scale at which this deviation occurs differs between methods. The grey curve (LT case) begins to decline beyond  $k \approx 0.04 h \text{ Mpc}^{-1}$  while for the NN case (blue), departures from unity are delayed until smaller scales ( $k \approx 0.07 h \text{ Mpc}^{-1}$ ). The LT+NN reconstruction (red curve) consistently provides the highest cross-correlation on all scales explored.

A notable feature of the NN reconstruction is the downturn of the cross-correlation coefficient on large scales, where both the LT and LT+NN methods perform better.

The origin of this loss of correlation at large scales is the same as that identified in the power spectrum analysis: the limited number of large-scale modes available in the 80 simulation boxes does not provide the NN method with sufficient information to effectively correct for redshift-space distortions on scales comparable to the survey volume.

This limitation does not affect the LT and LT+NN reconstructions, as their large-scale corrections rely on an approximate theoretical model of the system's dynamics rather than on a data-driven training set, which would require a much larger volume or more representative samples to capture those modes reliably.

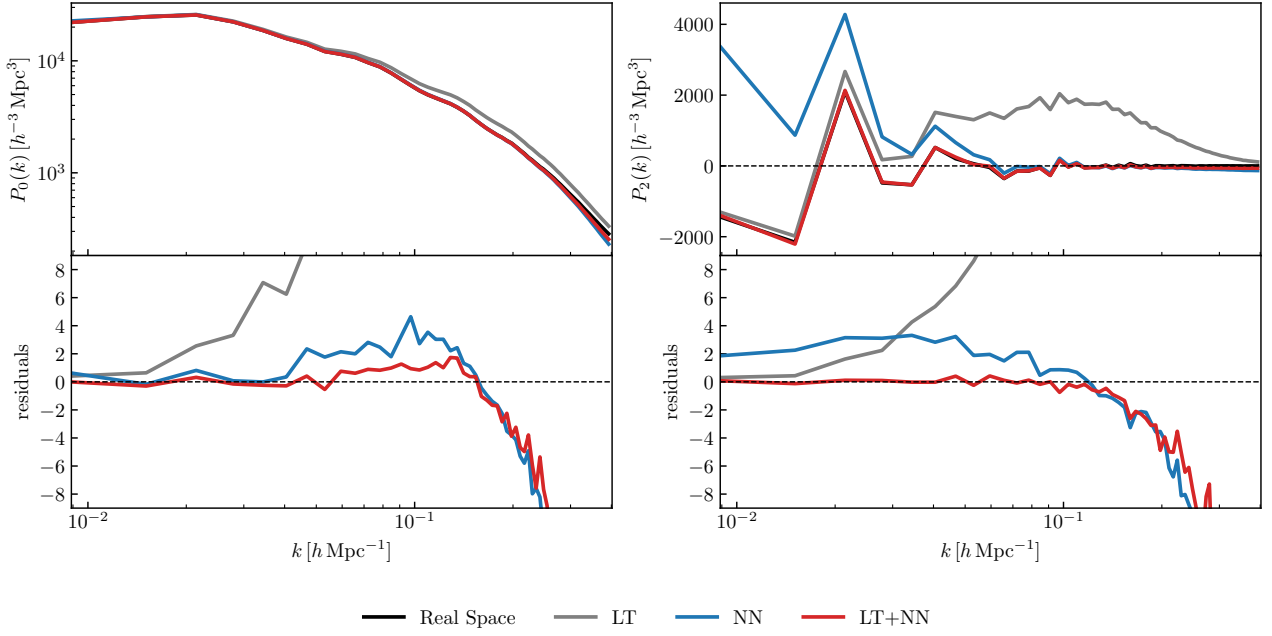


**Fig. 5.** Monopole and quadrupole moments of the power spectrum of the true and reconstructed halo number density fields, computed on  $128^3$  grids. In all cases, we show the average over the 20 validation fields. Different colors indicate different types of reconstructions, as specified in the figure legend. The left (right) panels display the monopole (quadrupole) moments in the top panels, and the corresponding residuals with respect to the reference (true) fields in the bottom panels. The grey bands in the bottom panels represent the  $1\sigma$  and  $2\sigma$  uncertainty regions, estimated from the scatter among the 20 realizations. LT and LT+NN reconstructions were performed using a Gaussian filter of radius  $R_s = 10 h^{-1} \text{Mpc}$ .

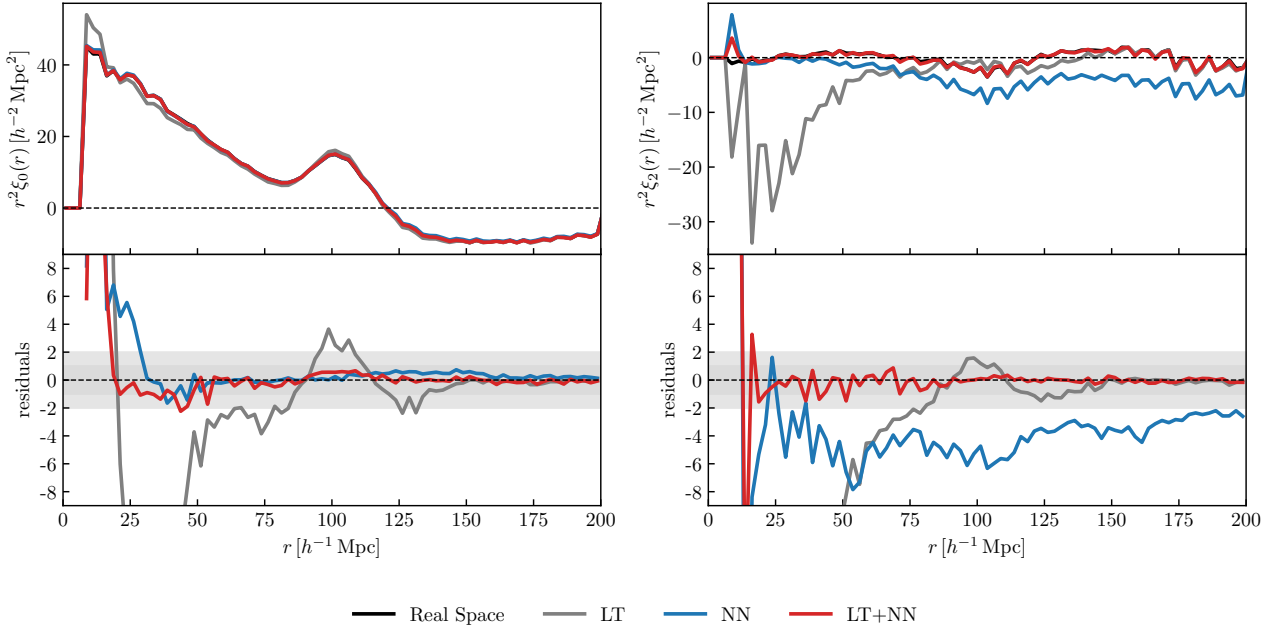


**Fig. 6.** Monopole (left panels) and quadrupole (right panels) moments of the halo 2PCF, averaged over the 20 reconstructions in the validation set. Curves in different colors correspond to the various reconstruction methods, as indicated in the figure legend. The top panels show the measured multipoles, while the bottom panels display the residuals with respect to the reference (true) case. Grey shaded bands indicate the  $1\sigma$  and  $2\sigma$  uncertainty regions, estimated from the scatter among the 20 realizations.

#### 4.3. Sensitivity to the smoothing scale

All reconstruction methods considered here use the same input: the halo number density field obtained by interpolating halo positions onto a  $128^3$  regular cubic grid. In two of the methods – LT and LT+NN – a Gaussian smoothing filter is applied before estimating the linear displacements of halos. The optimal choice

of the smoothing radius depends on the properties of the parent sample, particularly the tracer number density and the grid resolution. It may also vary depending on the specific analysis being performed.

In this section, we focus on the two-point halo–halo statistics by assessing the sensitivity of the reconstruction performance to the choice of the smoothing radius. For this test, we con-



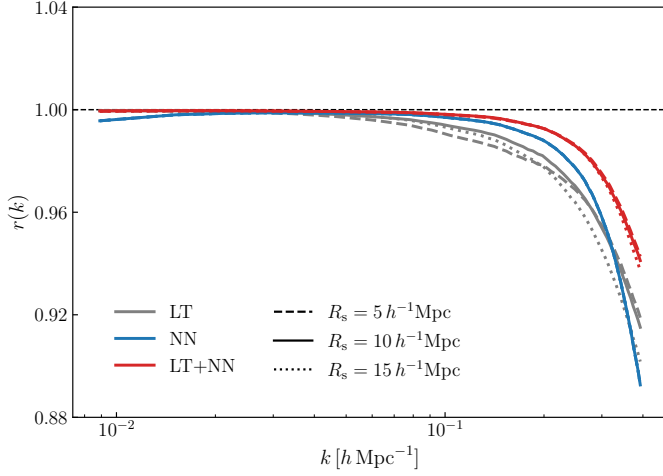


**Fig. 7.** Cross-correlation coefficient as a function of wavenumber between the reconstructed and true halo density power spectra. The curves represent averages over 20 realizations computed on a  $128^3$  grid. Different colors indicate the reconstruction methods, as specified in the labels. Different linestyles correspond to the smoothing radii used in the LT and LT+NN reconstructions, also detailed in the labels.

sider three smoothing scales, setting  $R_s = \{5, 10, 15\} h^{-1} \text{ Mpc}$ , and repeat the entire reconstruction procedure, including both training and validation, for each case. We then evaluate the impact of the smoothing scale on the mean squared error of the reconstructed fields and on the cross-correlation coefficient of the Fourier modes.

Fig. 8 shows, alongside with the same MSE curves shown in Fig. 1 (continuous line) for the reference  $R_s = 10 h^{-1} \text{ Mpc}$  case, the new ones obtained by performing LT and LT+NN reconstructions on the validation set with a smoothing radius of  $5 h^{-1} \text{ Mpc}$  (dashed) and  $15 h^{-1} \text{ Mpc}$  (dotted). For the LT case, decreasing the smoothing radius leads to a reduction in the MSE. This improvement arises because a smaller smoothing scale allows for a more accurate reconstruction of the displacement vectors. With  $R_s = 10 h^{-1} \text{ Mpc}$ , the displacement lengths were systematically underestimated, leading to an underestimation of the coherent RSD effect. This, in turn, caused an overestimation of the reconstructed halo overdensities and their two-point statistics. Decreasing the smoothing radius to  $R_s = 5 h^{-1} \text{ Mpc}$  mitigates this issue, while increasing it to  $R_s = 15 h^{-1} \text{ Mpc}$ , makes it worse.

The MSE curves for the LT+NN case lie well below those of the LT and NN reconstructions for all adopted smoothing values. Their asymptotic values decrease with decreasing smoothing length – a trend inherited from the LT step of the procedure, which, as discussed earlier, performs better when the smaller value  $R_s = 5 h^{-1} \text{ Mpc}$  is used. We note the peculiar shape of the MSE curve for the  $R_s = 5 h^{-1} \text{ Mpc}$  case, which closely follows that of the  $R_s = 10 h^{-1} \text{ Mpc}$  case up to around 400 training epochs, after which it suddenly drops. However, the fact that it flattens again after approximately 600 epochs suggests that overfitting is unlikely. Overall, the similarity of the MSE asymptotic values for the three smoothing filters considered indicate that the results of the LT+NN reconstruction are quite insensitive to the choice of the smoothing radius.

The analysis of the cross-correlation coefficients  $r(k)$  estimated for the LT reconstructions performed with the three smoothing filters, as shown in Fig. 7, corroborate this conclusion. The coefficients for the NN reconstruction (grey curves)

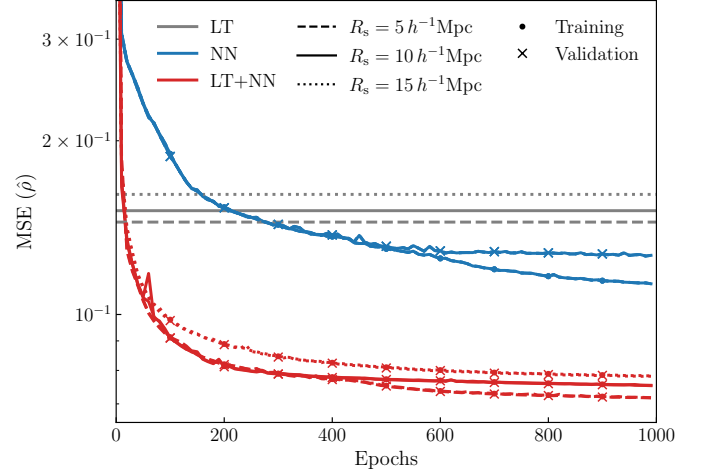


**Fig. 8.** MSE values estimated for the three types of reconstructions: LT, NN, and LT+NN. For the LT and LT+NN cases, results are shown for three different choices of the smoothing radius:  $R_s = 5 h^{-1} \text{ Mpc}$  (dashed curves),  $10 h^{-1} \text{ Mpc}$  (solid curves), and  $15 h^{-1} \text{ Mpc}$  (dotted curves). Dots and crosses indicate the values obtained from the training and validation sets, respectively.

show only mild sensitivity to the choice of smoothing scale. The addition of the NN step after the LT one not only increases the cross-correlation coefficient across all scales (with its lowest value at the Nyquist frequency still exceeding 0.93) but also makes the result remarkably insensitive to the adopted smoothing scale (red curves).

The impact of the smoothing scale on two-point statistics is, however, not negligible. Fig. 9, which mirrors the lower panel of Fig. 5, shows the residuals of the monopole (left) and quadrupole (right) moments of the average power spectra, computed from 20 reconstructions using the LT (grey), NN (blue), and LT+NN (red) methods with a smoothing radius of  $R_s = 10 h^{-1} \text{ Mpc}$ . Additionally, we show the corresponding residuals obtained by varying  $R_s$ , as indicated in the figure caption. While changes in the smoothing radius do not alter the overall trends, namely, LT systematically overestimates the amplitude of both moments on all scales (especially the small ones), and LT+NN consistently outperforms the other methods, the magnitude of the residuals is clearly affected by the choice of smoothing. Decreasing the smoothing radius improves the quality of the LT reconstruction, of both the quadrupole and the monopole, as one would have expected given the parallel improvement in the MSE.

The LT+NN case presents a more nuanced behaviour. Increasing (decreasing) the smoothing radius leads to a decrease (increase) in the amplitude of the monopole. This is similar to the LT case, which results in positive (negative) residuals relative to the reference case with  $R_s = 10 h^{-1} \text{ Mpc}$ . This occurs despite the cross-correlation coefficient remaining nearly constant across all smoothing values and the lowest MSE being achieved for  $R_s = 5 h^{-1} \text{ Mpc}$ . In contrast, the quadrupole moment appears less sensitive to the choice of smoothing radius. These findings reinforce the idea that the optimal smoothing filter depends on the specific statistical property of the density field being analyzed. A further example of this dependence will be discussed in the next section, where we consider cosmic voids.

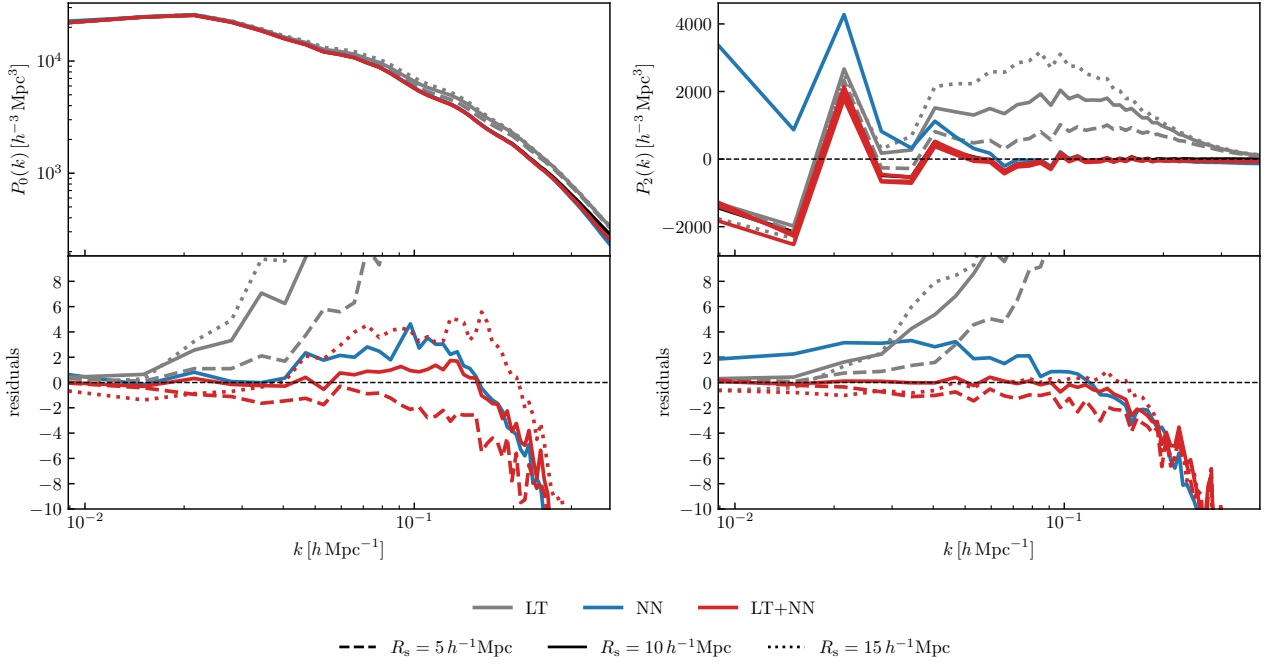


**Fig. 9.** Measurements and residuals of the monopole (left) and quadrupole (right) moments of the power spectrum of the true and reconstructed halo number density fields, computed on  $128^3$  grids and averaged over the 20 validation fields. The same color code is used consistently across all figures. Solid curves (see Fig. 5) correspond to the reference case with  $R_s = 10 h^{-1} \text{ Mpc}$ . Dashed and dotted curves represent reconstructions performed with  $R_s = 5 h^{-1} \text{ Mpc}$  and  $R_s = 15 h^{-1} \text{ Mpc}$ , respectively.

#### 4.4. The void-halo cross-correlation function

Cosmic voids, the underdense regions of the LSS, serve as valuable laboratories for extracting cosmological information. While BAO are well established as a standard ruler, cosmic voids can be considered standard spheres. This analogy arises from the cosmological principle, which states that the Universe is statistically isotropic and homogeneous on large scales.

A relatively novel approach in this context is the use of cosmic voids to perform cosmological tests. Although individual voids exhibit diverse and often irregular morphologies, their average shape, obtained by stacking many voids and averaging over all orientations, approximates spherical symmetry. This property allows voids to be employed as standard spheres in the Alcock–Paczynski test (Alcock & Paczynski 1979; Ryden 1995; Lavaux & Wandelt 2012; Sutter et al. 2014), which constrains cosmological parameters by measuring deviations from spherical symmetry in the observed void shapes. However, the AP signal is degenerate with RSDs, which induce anisotropic deformations in the observed shapes due to galaxy peculiar velocities.

The precision of the AP test can be significantly improved by applying reconstruction methods to mitigate redshift-space distortions before void identification in the galaxy distribution (Nadathur et al. 2019; Radinović et al. 2023).

Thus far, these studies have employed LT reconstruction techniques. In this section, we perform a similar analysis using, instead, the NN and hybrid LT+NN reconstruction methods, and compare the relative performance of the three approaches.

To perform this test, we considered the original 20 catalogs from the validation sample, along with their corresponding reconstructed versions using the LT, NN, and LT+NN methods. We applied the VIDE technique to all of them to identify cosmic voids (Sutter et al. 2015). VIDE is a publicly available package based on the ZOBOV algorithm (Neyrinck 2008), which uses a watershed transform applied to the density field derived from

the galaxy distribution via a Voronoi tessellation. The resulting void catalog provides, for each void, the spatial coordinates of its center and an effective radius  $r_v$ , which we use to rescale void sizes in order to estimate their mean density profile.

On average, the four resulting sets of void catalogs contain 7672 voids in real space, 7369 in the LT-reconstructed case, 7736 in the NN-reconstructed case, and 7645 in the LT+NN hybrid-reconstructed case. These values represent the mean over the 20 catalogs. Their similarity indicates that none of the reconstruction methods drastically alters the number of identified voids, and that the LT+NN approach most closely reproduces the real-space void count.

Next, we estimate the mean density profile of voids by computing, for each catalog, the monopole moment  $\xi_0(r)$  of the void-halo cross-correlation function. To this end, we use the estimator introduced by Davis & Peebles (1983):

$$\xi^{\text{DP}}(r, \mu) = \frac{n_R}{n_H} \frac{\mathcal{D}_v \mathcal{D}_h(r, \mu)}{\mathcal{D}_v \mathcal{R}_h(r, \mu)} - 1, \quad (10)$$

where  $\mathcal{D}_v \mathcal{D}_h(r, \mu)$  denotes the number of void–halo pairs at separation  $r$  and cosine of the angle  $\mu$  with respect to the line of sight to the pair. The line of sight is identified with the  $z$ -axis, which is aligned with one side of the cubic simulation box.  $\mathcal{D}_v \mathcal{R}_h(r, \mu)$  represents the number of void–random pair counts.  $n_R$  is the number of random halos homogeneously distributed throughout the box, and  $n_H$  is the number of true halos in the catalog. The separation  $r$  is a dimensionless quantity, defined by normalizing the void–halo pair separation by the effective radius of the void,  $r_v$ .

We evaluate  $\xi^{\text{DP}}(r, \mu)$  in 25 linearly spaced bins over the range  $r \in [0, 3]$  and in 100 linearly spaced bins over the range  $\mu \in [0, 1]$ . The resulting values are integrated over  $\mu$  to obtain the monopole moment  $\xi_0(r)$ . We also compute the quadrupole moment  $\xi_2(r)$ , which serves as an indicator of the effectiveness of

redshift-space distortion removal. In the absence of such distortions, as in real space, we expect the quadrupole signal to vanish. Therefore, deviations from a null quadrupole in redshift space reflect the presence of anisotropies, while the recovery of a zero quadrupole after reconstruction indicates successful suppression of RSD.

Fig. 10 presents the results of this analysis. On the left-hand side, we show the monopole moment of the cross-correlation function, i.e., the void density profile (top panel), and the residuals with respect to the reference real-space case (bottom panel), expressed in units of the *RMS* scatter.

In the LT-reconstructed case (grey curve), the central region of the void appears emptier than in the real-space reference. This is consistent with the results of the autocorrelation function test, which indicated that the LT method tends to over-correct for redshift-space distortions in the mildly non-linear regime, here manifesting as an overestimation of the matter outflow from void centers. The NN (blue curve), and especially the LT+NN (red curve), reconstructions perform significantly better. In both cases, the monopole of the cross-correlation function matches the true one within  $1\sigma$  (inner gray band).

Similar considerations apply to the quadrupole moment, shown in the right-hand panel of the same figure. The presence of a pronounced positive bump near the edge of the void in the LT-reconstructed quadrupole indicates that RSD are not successfully removed. Instead, the residual outflow induces a spurious elongation along the line-of-sight direction. The NN reconstruction performs significantly better, displaying a negative residual quadrupole signal that also peaks near the edge of the voids but remains below the  $2\sigma$  level of significance. This negative quadrupole is a signature of an underestimation of the outflow, related to the shallowness of the reconstructed voids, as previously seen in the monopole moment. The hybrid LT+NN reconstruction provides the best performance, removing redshift distortions almost perfectly across all scales.

In the LT case (grey curve) the central region of the void is emptier than expected. This is in accordance with the results of the autocorrelation function test which showed that LT over-corrects for RSD in the mildly linear regime, in this case by overpredicting the matter outflow from the voids. Conversely, the void profiles reconstructed using the neural network (NN) method more closely match the true central density, capturing the correct amplitude in the inner regions. The hybrid LT+NN method performs even better, yielding an excellent match to the real-space profile, particularly towards void centers.

## 5. Conclusions

In this work, we considered three different reconstruction methods and, using a set of simulated datasets, evaluated their ability to remove spurious anisotropies in the observed distribution of galaxies in spectroscopic redshift surveys – commonly known as redshift-space distortions (RSD). The three methods investigated are: (i) the so-called Zel’dovich reconstruction – a direct application of linear perturbation theory, commonly used to sharpen the BAO peak but employed here instead to model out RSD, which we refer to as LT; (ii) the method, introduced by Ganeshiah Veena et al. (2023) based on neural network reconstruction techniques, referred to as NN; and (iii) a novel hybrid approach, denoted LT+NN, in which a neural network is trained on LT-reconstructed fields.

To gauge the performance of the different methods, we rely on a set of 100 independent halo catalogs with a minimum mass

of  $1.64 \times 10^{12} M_{\odot} h^{-1}$ , extracted from the high-resolution QUIJOTE simulation suite. All realisations adopt the same fiducial cosmology but differ in their initial conditions. Each simulation box spans  $1000 h^{-1}$  Mpc on a side. In this work, we focus on the snapshot at redshift  $z = 1$ , as it corresponds to the typical redshift of Euclid and DESI, the largest spectroscopic galaxy surveys currently underway.

To quantitatively assess the quality of the reconstructions, we considered several indicators. First, we compared the true and reconstructed halo density fields at the nodes of a  $128^3$  cubic grid, evaluating the mean square error as well as the one-point probability distribution functions. Second, we analyzed two-point statistics in both Fourier and configuration space by comparing the measured two-point correlation functions and power spectra of the reconstructed fields with those of the true fields. To determine whether the phases, and not just the amplitudes, of the two-point statistics are accurately recovered, we also computed the cross-correlation of the Fourier coefficients. Finally, we focused on cosmic void statistics by computing the halo-void cross-correlation function, which allows us to assess the extent to which the reconstruction techniques restore the average spherical symmetry of voids.

The main results of our study are as follows

- Using the mean squared error (MSE) between the reconstructed and true density fields at each grid point, averaged over all grid points across all available catalogs, as a global proxy for reconstruction quality, we find that while the NN-based reconstruction performs marginally better than the LT method, achieving a 13 % reduction in MSE, it is the hybrid method that significantly improves the reconstruction quality, yielding a 50 % decrease in MSE. This is further confirmed by the high Pearson correlation coefficient of 0.98 between the reconstructed and true halo density fields obtained using the hybrid method.
- Examining the one-point probability distribution function of the reconstructed density field, we find that the LT+NN method provides the closest match to the true distribution across the entire density range. In contrast, the other two methods fail – each for different reasons – to accurately predict the PDF in the low-density tail and near the mean density, where the distribution peaks.
- Turning to two-point autocorrelation statistics, the LT+NN method again outperforms the other two across all scales larger than approximately  $25 h^{-1}$  Mpc, though for different reasons. The NN and hybrid methods perform equally well – and consistently better than LT – in reproducing the monopole of the true halo-halo correlation function on scales larger than  $40 h^{-1}$  Mpc (or, equivalently, for  $k < 0.2$ , in the power spectrum monopole). However, the NN method shows a systematically biased estimate of the quadrupole on all scales beyond  $25 h^{-1}$  Mpc. The presence of a negative residual quadrupole in the correlation function (and, correspondingly, a positive residual in the power spectrum) indicates that the NN method underestimates the amplitude of large-scale flows, failing to fully remove the spurious compression of structure along the line-of-sight direction. None of the reconstruction methods succeeds in recovering the two-point correlation properties of the halo field below  $20 h^{-1}$  Mpc. In the case of the NN and LT+NN methods, this failure likely reflects the finite size of the cubic grid used in the training and validation sets. This limitation could potentially be mitigated by reducing the grid size, albeit at the cost of increased computational burden.

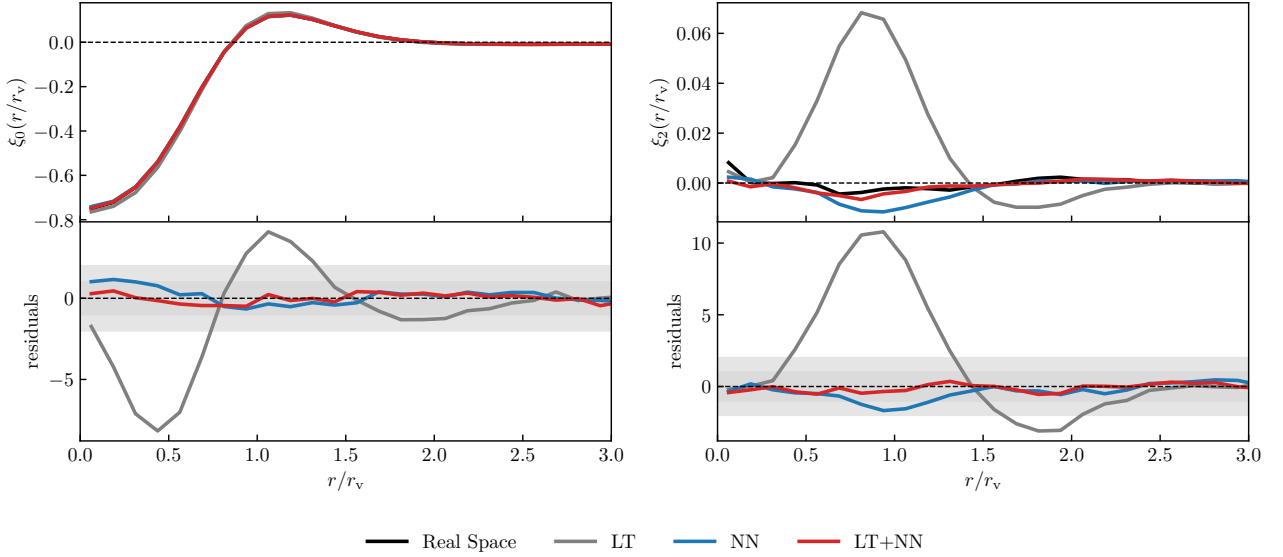


**Fig. 10.** Monopole (left panels) and quadrupole (right panels) moments of the void-halo cross correlation function, averaged over the 20 reconstructions in the validation set. Curves in different colors correspond to the various reconstruction methods, as indicated in the figure. The top panels show the measured multipoles, while the bottom panels display their residuals with respect to the reference case. Grey shaded bands indicate the  $1\sigma$  and  $2\sigma$  uncertainty regions, estimated from the scatter among the 20 realizations.

- The superiority of the LT+NN method is further demonstrated by its excellent recovery of the phases of the density field, as shown by the cross-correlation between truth and reconstructed fields. It remains accurate out to wavenumbers as large as  $k = 0.2 h \text{ Mpc}^{-1}$ . It outperforms both LT, which fails on small scales, and NN, which instead underperforms on large scales. This is an interesting result which, together with the findings from the two-point correlation analysis, illustrates that the success of the hybrid approach relies on the synergy between the combined methods. The NN approach is successful in removing redshift-space distortions on relatively small scales, where methods based on linear theory tend to fail. This is because, on small scales, a large number of Fourier modes are available – even with a relatively modest number of realizations in the training set – allowing the NN to learn effectively. Conversely, due to the limited number of large-scale Fourier modes in the training data, the NN fails on large scales, where the LT method succeeds.
- Since accurate RSD removal is also important for effectively using cosmic voids as cosmological probes, we have tested the ability of the three reconstruction methods to recover the correct void density profile, measured by the void-halo two-point correlation function, and their average spherical shape, assessed via the quadrupole moment of the same quantity. Voids reconstructed by the LT methods are emptier than expected and exhibit an overdensity ridge that is more prominent than it should be. Both features result from an overprediction of the velocity outflow, which also artificially elongates these structures, as indicated by the positive residual quadrupole. Both the NN and LT+NN methods perform significantly better, with the latter yielding a closer match to the expected void density profile and a quadrupole moment that remains remarkably close to zero across all scales considered.
- The same halo density field, specified on a  $128^3$  cubic grid, is used as input for all three reconstruction methods. However, the LT and LT+NN methods apply an additional Gaussian smoothing filter prior to estimating halo displacements. The

optimal smoothing radius depends on the mean tracer density, the grid resolution, and potentially on the type of probe considered for the cosmological analysis.

We evaluated the sensitivity of our results to the smoothing scale by repeating the reconstructions with different smoothing radii. Focusing on the two-point correlation analysis, we found that while the LT method exhibits a strong dependence on the choice of filter, the hybrid method is significantly more robust. In particular, the stability of the quadrupole moment across smoothing scales suggests that the LT+NN approach effectively removes spurious anisotropies and is remarkably insensitive to the specific smoothing procedure employed.

Furthermore, the ability of the hybrid method to accurately recover the cosmic void profile and shape using the same smoothing radius adopted in the halo-halo correlation analysis is especially encouraging. This consistency indicates that a single smoothing filter can be applied across different probes without introducing significant bias. The robustness of the LT+NN method to the choice of smoothing – confirmed by repeating the void analysis on a single halo catalog with various smoothing scales – is a key advantage, and contrasts with the sensitivity observed in the LT method.

In summary, our results show that the novel hybrid method presented in this work consistently outperforms the two baseline methods that rely on only one of the two underlying strategies when applied to a sample of mass tracers at  $z = 1$ .

Parker et al. (2025) applied a similar hybrid approach to reconstruct the early Universe’s mass density field from later-time tracers. In contrast, we focus on a more modest yet crucial task: removing redshift-space distortions from observed tracer distributions.

Our results underscore the power of combining neural networks with traditional dynamical modeling to extract cosmological information from large-scale structure surveys. While promising, these results are based on idealized data. Testing the hybrid method on real surveys is essential, but the outlook is encouraging.



Wide-field surveys often suffer from fragmented footprints, irregular edges, and masked regions. Neural networks have already shown strong performance in handling such issues, interpolating missing data and extrapolating near boundaries (Lilow et al. 2024). Moreover, spectroscopic surveys also face complex, spatially varying selection functions. Here too, neural networks—especially self-organizing maps, originally used in photometric redshift estimation (e.g., Carrasco Kind & Brunner 2014), offer a path forward, now being repurposed to assess spectroscopic survey purity.

Galaxy bias presents another key challenge. We modeled biased tracers as halos, but real surveys target specific galaxy types. Ideally, networks should be trained on realistic mocks matching survey properties. Alternatively, bias correction could be built into the hybrid pipeline. Parker et al. (2025) highlight the need for added features like host halo mass to improve reconstruction fidelity.

Whether these complexities, bias, selection effects, survey geometry, can be fully addressed within an LT+NN (or a NN–LT–NN) hybrid framework remains an open question, and one we intend to pursue.

Whether all of these complexities can be effectively addressed within an LT+NN (or potentially NN–LT–NN) hybrid framework is an open question and one we plan to explore in future work.

*Acknowledgements.* The authors thank A. Veropalumbo for helpful comments and support with the measurements of clustering statistics. PGV thanks R. Lilow for discussions. EM, PGV and EB thank A. Nusser and R. Sheth for their useful comments. PGV and EB are supported by MIUR/PRIN 2022 "Optimal cosmology with next generation galaxy surveys". EM and EB are also supported by ASI/INAF agreement "Scientific activity for Euclid mission, Phase E". GD acknowledges support from the french government under the France 2030 investment plan, as part of the Initiative d'Excellence d'Aix-Marseille Université - A\*MIDEX AMX-22-CEI-03

## References

- Alcock, C. & Paczynski, B. 1979, *Nature*, 281, 358  
 Burden, A., Percival, W. J., & Howlett, C. 2015, *MNRAS*, 453, 456–468  
 Carrasco Kind, M. & Brunner, R. J. 2014, *MNRAS*, 438, 3409  
 Chen, B.-Q., Qin, F., & Li, G.-X. 2024, *MNRAS*, 528, 7600  
 Chen, X., Zhu, F., Gaines, S., & Padmanabhan, N. 2023, *MNRAS*, 523, 6272–6281  
 Davis, M. & Peebles, P. J. E. 1983, *ApJ*, 267, 465  
 DESI Collaboration, Abdul-Karim, M., Aguilar, J., et al. 2025, DESI DR2 Results II: Measurements of Baryon Acoustic Oscillations and Cosmological Constraints  
 Dore, O., Hirata, C., Wang, Y., et al. 2019, arXiv preprint arXiv:1904.01174  
 Du, W., Luo, X., Jiang, Z., et al. 2025, arXiv e-prints, arXiv:2504.06309  
 Eisenstein, D. J., Zehavi, I., Hogg, D. W., et al. 2005, *The Astrophysical Journal*, 633, 560  
 Frisch, U., Matarrese, S., Mohayaee, R., & Sobolevski, A. 2002, *Nature*, 417, 260–262  
 Ganeshaiah Veena, P., Lilow, R., & Nusser, A. 2023, *MNRAS*, 522, 5291–5307  
 Goodfellow, I., Bengio, Y., & Courville, A. 2016, *Deep Learning* (Cambridge, Massachusetts: MIT Press)  
 Hamilton, A. J. S. 1998, *Linear Redshift Distortions: A Review* (Springer Netherlands), 185–275  
 Hand, N., Li, Y., Slepian, Z., & Seljak, U. 2017, *J. Cosmology Astropart. Phys.*, 2017, 002  
 Hong, S. E., Jeong, D., Hwang, H. S., & Kim, J. 2021, *ApJ*, 913, 76  
 Ivezić, Z., Kahn, S. M., Tyson, J. A., et al. 2019, *The Astrophysical Journal*, 873, 111  
 Jackson, J. C. 1972, *MNRAS*, 156, 1P  
 Kaiser, N. 1987, *MNRAS*, 227, 1  
 Lavaux, G. & Wandelt, B. D. 2012, *ApJ*, 754, 109  
 Lilow, R., Ganeshaiah Veena, P., & Nusser, A. 2024, *A&A*, 689, A226  
 Mellier, Y., Abdurro'uf, Acevedo Barroso, J. A., et al. 2025, *A&A*, 697, A1  
 Nadathur, S., Carter, P. M., Percival, W. J., Winther, H. A., & Bautista, J. E. 2019, *Phys. Rev. D*, 100, 023504  
 Neyrinck, M. C. 2008, *MNRAS*, 386, 2101

- Nikakhtar, F., Padmanabhan, N., Lévy, B., Sheth, R. K., & Mohayaee, R. 2023, *Optimal Transport Reconstruction of Biased Tracers in Redshift Space*  
 Nusser, A. & Davis, M. 1994, *ApJ*, 421, L1  
 Padmanabhan, N., Xu, X., Eisenstein, D. J., et al. 2012, *MNRAS*, 427, 2132–2145  
 Paillas, E., Ding, Z., Chen, X., et al. 2025, *Journal of Cosmology and Astroparticle Physics*, 2025, 142  
 Parker, L., Bayer, A. E., & Seljak, U. 2025, *Initial Conditions from Galaxies: Machine-Learning Subgrid Correction to Standard Reconstruction*  
 Peebles, P. J. E. 1989, *ApJ*, 344, L53  
 Radinović, S., Nadathur, S., Winther, H. A., et al. 2023, *A&A*, 677, A78  
 Ryden, B. S. 1995, *ApJ*, 452, 25  
 Sarpa, E., Schimd, C., Branchini, E., & Matarrese, S. 2019, *MNRAS*, 484, 3818–3830  
 Shallue, C. J. & Eisenstein, D. J. 2023, *MNRAS*, 520, 6256  
 Shi, F., Wang, Z., Yang, X., et al. 2025, arXiv e-prints, arXiv:2501.12621  
 Sutter, P. M., Lavaux, G., Hamaus, N., et al. 2015, *Astronomy and Computing*, 9, 1  
 Sutter, P. M., Pisani, A., Wandelt, B. D., & Weinberg, D. H. 2014, *MNRAS*, 443, 2983  
 Villaescusa-Navarro, F., Anglés-Alcázar, D., Genel, S., et al. 2021, *ApJ*, 915, 71  
 Villaescusa-Navarro, F., Hahn, C., Massara, E., et al. 2020, *ApJS*, 250, 2  
 Wang, Y. & Yang, X. 2024, *ApJ*, 969, 76  
 White, M. 2015, *MNRAS*, 450, 3822–3828  
 Wu, Z., Xiao, L., Xiao, X., et al. 2023, *MNRAS*, 522, 4748  
 Zel'dovich, Y. B. 1970, *A&A*, 5, 84